ORIGINAL ARTICLE

Numerical calculation of FSS/RSS transition in highly overexpanded rocket nozzle flows

Emanuele Martelli · Francesco Nasuti · Marcello Onofri

Abstract Turbulent flow separation in over-expanded rocket nozzles is investigated numerically in a sub-scale parabolic nozzle fed with cold nitrogen. Depending upon the feeding to ambient pressure ratio either a free shock separation or a restricted shock separation is computed, with a significant hysteresis between these two flow regimes. This hysteresis was also found in experimental tests with the same nozzle geometry. The present study is mainly focused on the transition between the two shock separation patterns. The analysis of the numerical solutions aims to provide clues for the explanation of the hysteresis cycle.

Keywords Rocket nozzle · Flow separation · Hysteresis

1 Introduction

The structure of the liquid rocket engine nozzle flow field generated by the flow separation that occurs because of a strong overexpansion has attracted many experimental and numerical studies [1–11]. The reason why so many studies

E. Martelli (✉)
Dip. Ing. Aerospaziale e Meccanica,
II Univ. degli Studi di Napoli, Via Roma 29,
81031 Aversa (CE), Italy
e-mail: emanuele.martelli@unina2.it;
emanuele.martelli@uniroma1.it

F. Nasuti · M. Onofri
Dip. Meccanica e Aeronautica, Univ. Roma "La Sapienza",
Via Eudossiana 18, 00184 Rome, Italy
e-mail: francesco.nasuti@uniroma1.it

M. Onofri
e-mail: marcello.onofri@uniroma1.it

have been carried out on this subject is that the evolution of flow separation structures during nozzle startup and shutdown seems to be the main responsible for the generation of large lateral forces.

The flow separation structures are characterized by different Mach reflections of the separation shock [12]. In fact, flow separation in supersonic nozzles is accompanied by an oblique shock necessary to permit the supersonic flow to deviate and increase its pressure to adapt to the ambient condition. The separation shock always reflects on the nozzle axis by a Mach reflection, however, this Mach reflection can show a flat or a curved Mach disk, depending on the properties of the flow upstream. It is worth noticing that, for thrust optimized contour nozzles and thrust optimized parabolic nozzles, the large radial flow gradients ahead of the Mach disk, which are carried out by the internal shock propagating from the throat region of these nozzles, yield a curvature of the Mach disk strong enough to produce a large vortex in the core of the nozzle exhaust jet. The occurrence of this vortex, also referred to as "inviscid separation" to emphasize its origin related to vorticity generated by shock curvature rather than to boundary layer separation [2], has been considered questionable for a long time and only recently has been proved by experimental tests [13,14]. The existence of a large recirculating flow region in the nozzle exhaust jet is not important per se. Rather, it is important for nozzle design especially because it is accompanied with a deviation of the supersonic jet towards the wall that can lead to flow reattachment. Experimental and numerical studies have led to the common understanding that the highest side loads take place when the flow structure inside the nozzle passes from a condition with the typical separated flow [free shock separation (FSS)] to a condition featuring the more unusual flow separation and reattachment [restricted shock separation (RSS)] [15–17]. Moreover, an hysteresis range in the Mach reflection

has been found both numerically and experimentally in different configurations, like the J-2S sub scale nozzle and the Vulcain nozzle [1], indicating that transition between FSS and RSS occurs at a different pressure ratio (PR) depending if PR is increasing (startup phase) or decreasing (shutdown phase).

In the present study the startup and shutdown phases of a sub-scale parabolic nozzle are simulated considering a series of steady state solutions. The main goal is to look for the existence of multiple solutions for overexpanded flows at the same PR, by computations which start from different initial conditions. These computations aim to verify the width of the hysteresis range and to provide clues for understanding the reason leading to different values of the PR for the transition and re-transition between FSS and RSS.

2 Numerical approach and validation test cases

The analysis of the nozzle flow field is performed by a 2D axisymmetric time-accurate perfect gas Reynolds averaged Navier–Stokes solver, based on the approach described in [18]. The main features of this method are to discretize the convective terms according to the lambda scheme developed by Moretti [19]. The discontinuities are solved via a finite volume Godunov method (hybrid formulation [20]). The viscosity is described by Sutherland's law. Turbulence is computed by the Spalart and Allmaras [21] one-equation model. To verify the capabilities of the numerical tool in predicting the actual flow separation structure in overexpanded nozzles, two validation test cases have been considered. The first test case is a truncated ideal contour (ATAC-TIC) sub-scale nozzle showing a FSS flow structure, while a sub-scale parabolic nozzle (VAC-S1) is considered as a RSS validation test case. Both simulations are characterized by a computational domain including the nozzle and an external region at its exit wide enough to simulate the nozzle discharge in a constant pressure ambient. The enforced boundary conditions are indicated in Fig. 1, subsonic inflow at the nozzle feeding chamber (total temperature and total pressure are enforced together with the flow direction), symmetry axis, adiabatic wall, subsonic inflow boundary condition on the left side of the external region (main flow direction is from left to right), assigned pressure and non-reflecting boundary conditions on the upper and on the right side, respectively.

2.1 FSS validation test case

The ATAC-TIC nozzle geometry, operating conditions (working gas, feeding pressure and temperature) and experimental data are taken from [22], which describes the results of a workshop, where the results computed with the present solver are compared with experimental data and other
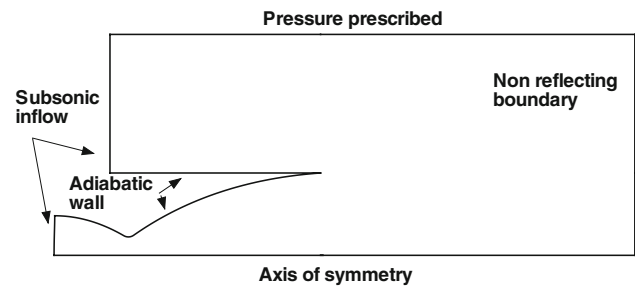

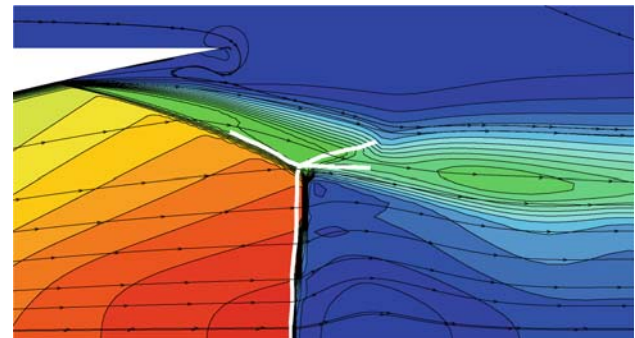**Fig. 1** Computational domain and assigned boundary conditions

Fig. 2 ATAC-TIC nozzle at PR = 25; *white lines* experimental shock position

Table 1 ATAC-TIC grid resolution

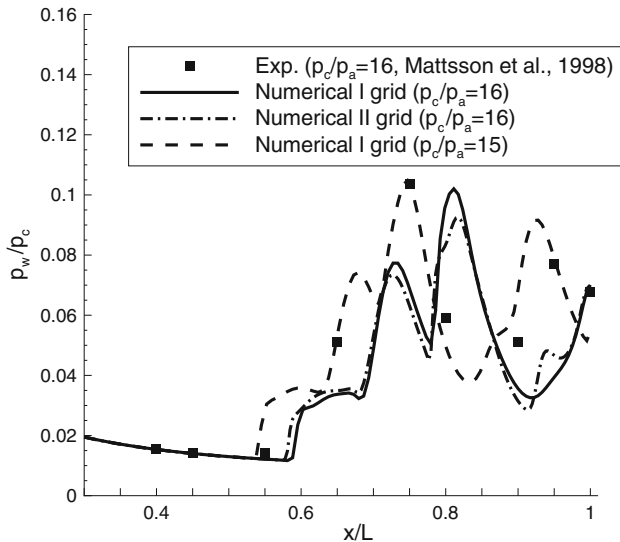| Grid level	Inside nozzle	Total
I	240×60	24,000
II	480×120	72,000

computations, showing a good prediction capability. As an example, Fig. 2 shows the Mach number flow field at the exit section of the ATAC-TIC nozzle at a pressure ratio PR = $p_c/p_a = 25$, obtained with the second grid level reported in Table 1. The numerical prediction of the shock position is in very good agreement with the experimental one, shown by the white lines in the figure. In particular the position of the triple point is well captured.

2.2 RSS validation test case

The geometric, operating and experimental data of the selected parabolic nozzle can be found in [23]. The computational grid data are reported in Table 2. The results for the parabolic nozzle are summarized in Fig. 3, by comparison with the experimental wall pressure data at PR = 16. Grid independence of these results is also shown in Fig. 3. However, as the present comparison shows, the computed separation point at PR = 16 is placed downstream with respect to the measured position. It is interesting to note that the

Table 2 VAC-S1 grid resolution

Grid level	Inside nozzle	Total
I	240×120	38,400
II	480×240	124,800

Fig. 3 VAC-S1 nozzle at PR = 16: wall pressure profile

Fig. 4 VAC S1 Mach number flow field; *up* $p_c/p_a = 14$, RSS; *down* $p_c/p_a = 10$, FSS. Shock nomenclature: *a* internal shock; *b* Mach disk; *c* reflected shock; *d* separation shock

qualitative behavior of the RSS pattern is well captured by the numerical simulations, as it can be seen by comparison of the numerical solution at PR = 15 with the experimental data taken at PR = 16. The discrepancy is not surprising as the prediction of the separation is directly connected to turbulence modeling, which is responsible of the large differences in the prediction of the separation point, as shown for instance in [22,25].

3 Transition between FSS and RSS

The analysis of the change in the shock separation structure is carried out for the parabolic VAC-S1 nozzle. This geometry has been selected because it shows both flow separation structures and because both experimental and numerical data are reported in [23]. The FSS and RSS computed shock separation patterns are shown in Fig. 4. At PR = 10, the FSS pattern is computed, the boundary layer separates and never re-attaches to the wall. At PR = 14, the RSS pattern is obtained, the flowfield is characterized by the re-attachment of the boundary layer to the wall, with the formation of a closed recirculation bubble (the supersonic separated jet is confined by the wall).

Because the transition between FSS and RSS is governed by the PR, successive steady state solutions for different given PR are computed. Each PR computation uses the

previous flow field as initial conditions. This choice does not affect the shock pattern transition results, because the characteristic time scale of the chamber pressure variation in a real hardware is much longer than the gasdynamic characteristic time scale. Therefore, it is a good approximation to study the transition by a series of steady state solutions. In [24], the transition between the FSS and the RSS in a parabolic nozzle is reported considering a time accurate analysis of the inlet history based on an engine system simulation. The importance of the time accurate analysis emerges when the computation of the side loads is the primary goal.

In the following, the term up-ramping indicates a sequence of steady state computations starting from PR = 8 and obtained by increasing the PR at each step. The predicted wall pressure behavior during the up-ramping is shown in Fig. 5. Similarly, the term down-ramping indicates a sequence of steady state solutions computed starting from PR = 16 and decreasing the PR step by step down to the value of 7 (Fig. 6). The transition between FSS and RSS can be identified in Figs. 5 and 6 by the abrupt change in the wall pressure behavior. The computed FSS/RSS transition occurs for PR > 13 during the up-ramping and the re-transition for PR < 8 during the down-ramping. Therefore, a significant hysteresis range takes place which will be analyzed in the following.

3.1 Free shock separation

In the FSS case the wall pressure evolution is mainly governed by the classical supersonic flow separation [26]. The first deviation of the wall pressure from the vacuum profile is commonly defined as incipient separation pressure p_i. Then the wall pressure quickly rises to a plateau pressure p_p, which represents the pressure in the subsonic recirculating
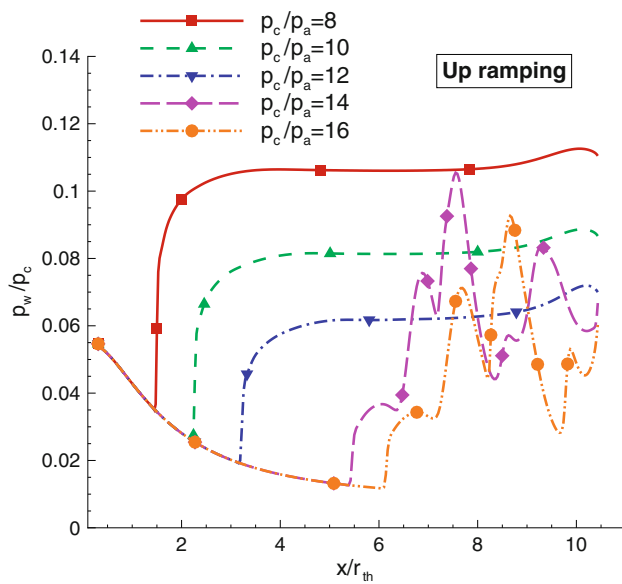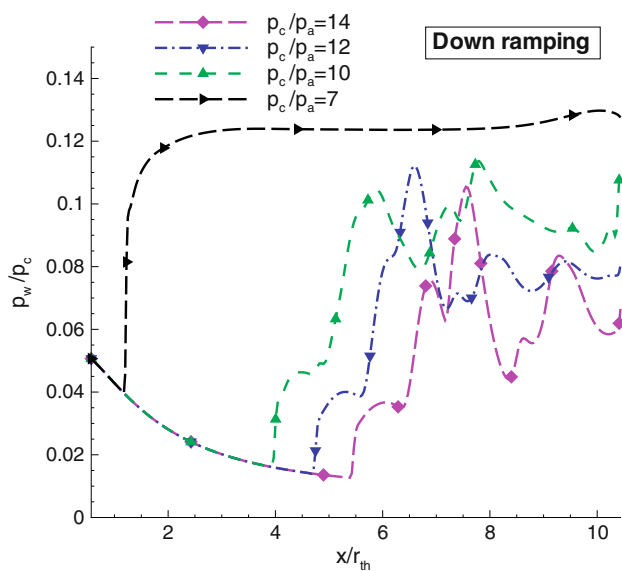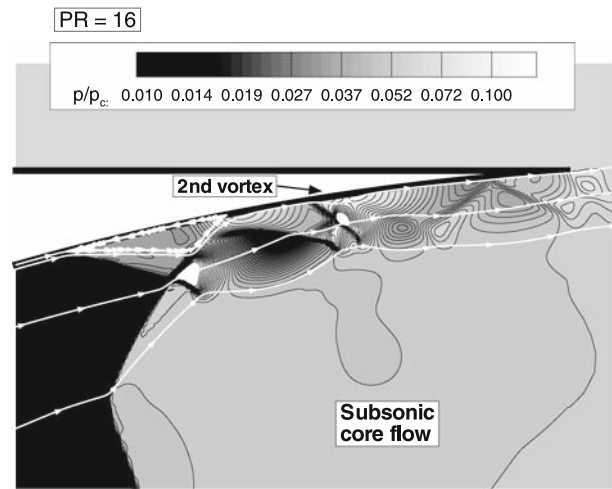
Fig. 5 Wall pressures during the up-ramping

Fig. 7 VAC S1 static pressure flow field

jet [16]). As a consequence of this lower value there is a downstream (upstream) jump of the separation point after the transition, as shown in Figs. 5 and 6. The main features of the shock pattern are shown in Fig. 4. The internal shock (a), originating from the change of curvature between the throat and the parabolic section, interacts with the Mach disk (b) before its reflection on the axis of symmetry. As a consequence of this shock/shock interaction there is a sudden change in the shape of the Mach disk [12], a triple point is formed by the interaction of the internal shock (a), the Mach disk (b) and the reflected shock (c) (Fig. 4). The re-attached supersonic jet undergoes a series of shocks and expansions, whose number depends on the separation point location, to adapt to the ambient pressure and this explains the oscillating wall pressure behavior, with the highest peak greater than the ambient pressure. Figure 7 shows an enlargement of the static pressure field in the re-attachment region at PR = 16, and Fig. 8 shows the shocks in the supersonic confined jet. As can be seen from the pictures, the whole flow structure can be interpreted as a series of shock/boundary layer interactions, where the reflected shock (c) in Fig. 8, acts as an incident shock and impinges on the wall causing the boundary layer separation and the first separation shock (d). As the reflected shock (c) penetrates in the boundary layer it becomes less intense, changes curvature and originates an expansion wave. Through this expansion the streamlines deviate toward the wall, causing the re-attachment of the boundary layer to the wall and the rise of the re-attachment shock (e). Then the expansion wave reflects as a shock when it impinges on the subsonic region of the core flow, which behaves like a constant pressure region. This reflected shock becomes a new incident shock (c1), which generates a second separation bubble. The sequence repeats again a third time, but due to the lower supersonic Mach number the shock is not intense enough to generate a third recirculation bubble and there is a
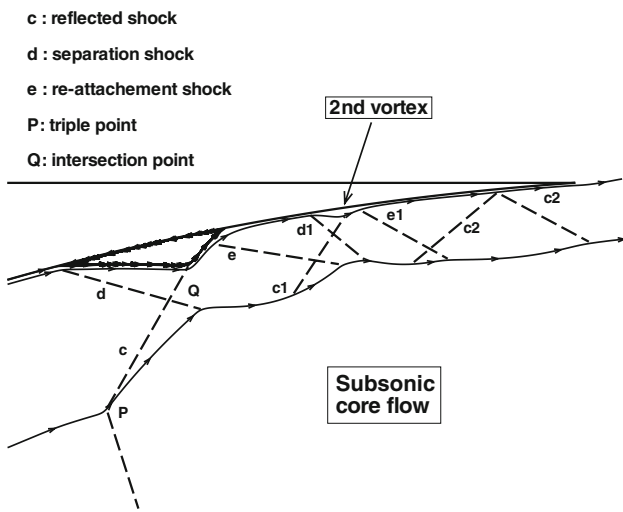

Fig. 6 Wall pressures during the down-ramping

separated region and is, therefore, slightly lower than the ambient pressure p_a. The resulting flow structure is that shown if Fig. 4, where the main shocks branches can be easily identified: the Mach disk (b), the reflected shock (c) and the separation shock (d).

3.2 Restricted shock separation

In the RSS case, a closed separation zone is formed with a plateau pressure significantly below the ambient pressure (the bubble is isolated from the ambient by the supersonic

c : reflected shock

d : separation shock

e : re-attachment shock

P: triple point

Q: intersection point

Fig. 8 Shocks experienced by the supersonic confined jet
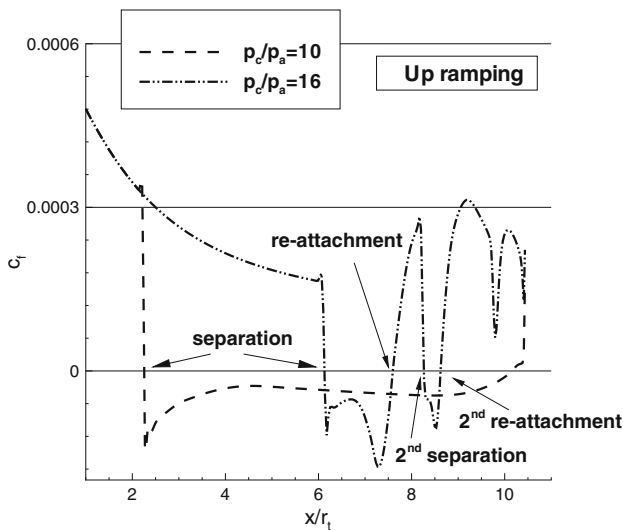
Fig. 9 Wall friction coefficient, PR = 10 and 16 (up-ramping)

Fig. 10 Non-dimensional separation point abscissa x_i/r_{th} versus pressure ratio PR

3.3 Hysteresis phenomenon

In the experiments carried out with the VAC-S1 geometry [23], it has been shown that the transition between free and RSS presents an hysteresis phenomenon, the transition from FSS to RSS occurs at a higher PR than the one observed for the re-transition from RSS to FSS. The hysteresis cycle has been obtained in the VAC-S1 by the present numerical simulations (Figs. 5, 6). The effect of the grid resolution on the results is shown in Fig. 10, by comparing the separation point abscissas, normalized with the throat radius x_i/r_{th}, obtained at various PR with the two grid levels reported in Table 2. The FSS structure was obtained by increasing the PR up to 12, step by step (PR = 8, 10, 12). The transition from FSS to RSS appears when the PR increases from 12 to 13. Then the RSS pattern becomes the stable flow structure, which remains also if PR is decreased down to the value of 8. Only a further decrease from 8 to 7 switches the separation structure back to FSS. The result is that there is a range of PR where two possible solutions exist. This range is referred to as hysteresis range. The numerical simulations provide a shifted range with respect to the experimental one: $8 \leq PR \leq 12$ (present results) and $13 \leq PR \leq 15$ (experimental data [23]). This disagreement could be due to the turbulence model, as already stated in the RSS validation section. The analysis of the separation point abscissa (x_i/r_{th}) versus the PR (Fig. 10) also shows that there is a linear correlation between these two variables, which was found experimentally for a sub-scale truncated ideal nozzle [28]. It is interesting to note that,

shock reflection without separation. The existence of multiple recirculation bubbles can also be analyzed by looking at the wall friction coefficient (c_f, Fig. 9). For PR = 10 (FSS) the c_f becomes negative at the separation point and at the nozzle lip positive again due to the separation of the back flow from the ambient. At PR = 16 (RSS), the c_f behavior shows two separation and two re-attachment points and that the second bubble is smaller than the first one. The existence of different recirculation regions was confirmed experimentally by visualizations by means of coatings in a sub-scale parabolic nozzle similar to the VAC-S1 [27]. As discussed in [27], the evacuation of these bubbles during the startup phase is correlated to the appearance of lateral forces.
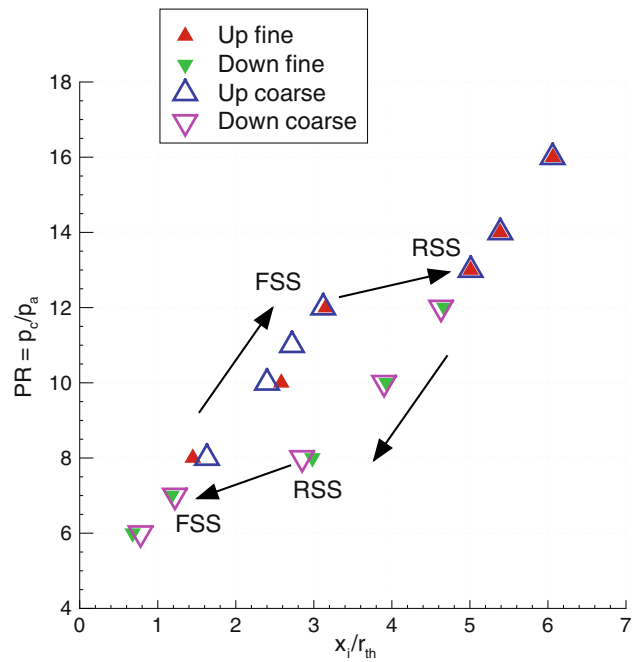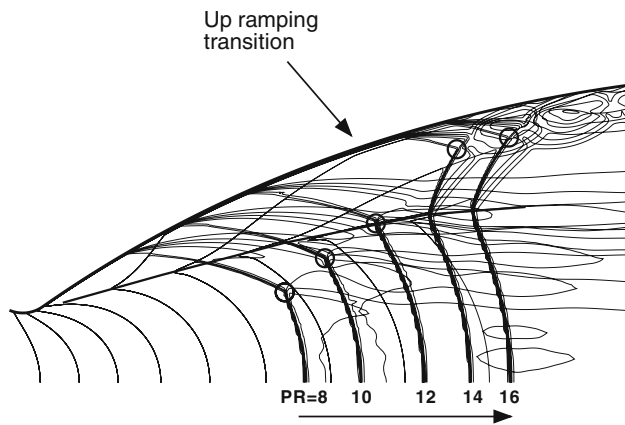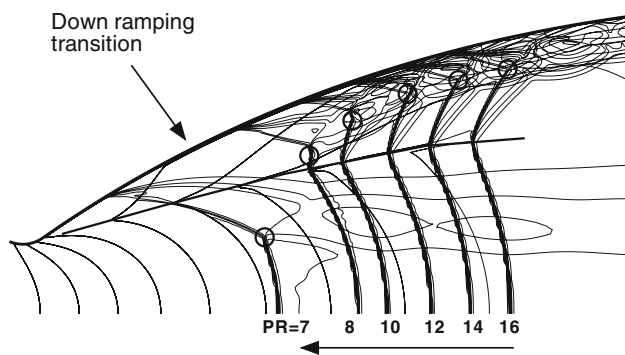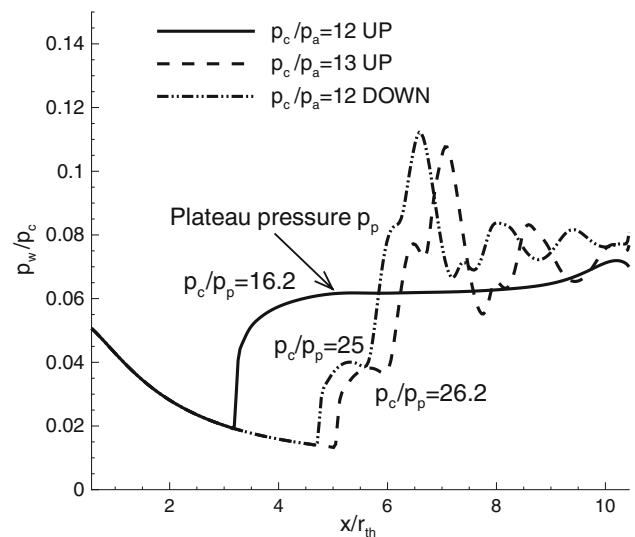
Fig. 11 VAC S1 Mach number contour lines during the up-ramping

Fig. 12 VAC S1 Mach number contour lines during the down-ramping


Fig. 13 VAC S1 wall pressure

because of the hysteresis, there are two distinct linear trends, one for FSS and one for RSS, with similar inclination.

A possible interpretation of the existence of the hysteresis range can be inferred from the analysis of the computed data. To this goal the Mach number contour lines obtained at different PR during the up-ramping and the down-ramping are superimposed in Figs. 11 and 12, respectively, where the internal shock position is emphasized by a black line. During the up-ramping the transition from FSS to RSS occurs when the internal shock intersects the separation shock below the triple point. In fact, if the intersection point is above the triple point the internal and the separation shocks are of the same family and coalesce. On the other hand if the intersection point is below the triple point the internal shock intersects the Mach disk and the up stream radial gradient changes the Mach reflection curvature with the downstream jump of the separation point. During the down-ramping (Fig. 12) the re-transition occurs in a similar manner: when the intersection point (Q in Fig. 8) between the reflected shock (c) and the separation shock (d) reaches the internal shock (a), the Mach reflection changes configuration again and the FSS pattern is obtained, with the upstream jump of the separation point. This downstream or upstream sudden movement

is important in order to understand the hysteresis phenomenon. Figure 13 shows the wall pressure for PR = 12 and 13 (up-ramping) and for PR = 12 (down-ramping), so as to compare both FSS and RSS solutions at PR = 12 and RSS at PR = 13. The ratios between the chamber pressure p_c and the plateau pressure p_p for each solution shows that the plateau pressure is slightly below the ambient value in case of FSS and much lower than the ambient pressure in case of RSS. Therefore, the sequence PR = 12, 13, 12 corresponds to the sequence PR_p = 16.2, 26.2, 25, where $PR_p = p_c/p_p$. This helps explaining the hysteresis: the separation point position depends on the value of the plateau pressure ratio PR_p rather than on the nominal pressure ratio PR. Therefore, two different PR_p with two different correlated positions of x_i can correspond to the same nominal PR. Figure 14 shows that if the separation point abscissas are plotted versus PR_p the data collapse on a single linear correlation and that for $x_i/r_{th} < 3$ (approximately) there are only FSS solutions (FSS domain), while for $x_i/r_{th} > 3$ there are only RSS solutions (RSS domain). It is also possible to observe that during the up-ramping the solutions can cover all the positions in the FSS domain. When the separation point enters the RSS domain there is a jump in terms of x_i and PR_p due to the transition from FSS to RSS. In a similar way, during the down-ramping the solutions can cover all the positions in the RSS domain. When the separation point enters the FSS domain there is again a jump of PR_p and an upstream jump of the separation point due to the re-transition from RSS to FSS. The no-solution regions, one in the RSS domain during the up-ramping and one in the FSS domain during the down-ramping, are responsible for the presence of the hysteresis. Finally, due to the single-valued relationship between x_i and PR_p, a single transition point can be individuated around $PR_p = 15$.
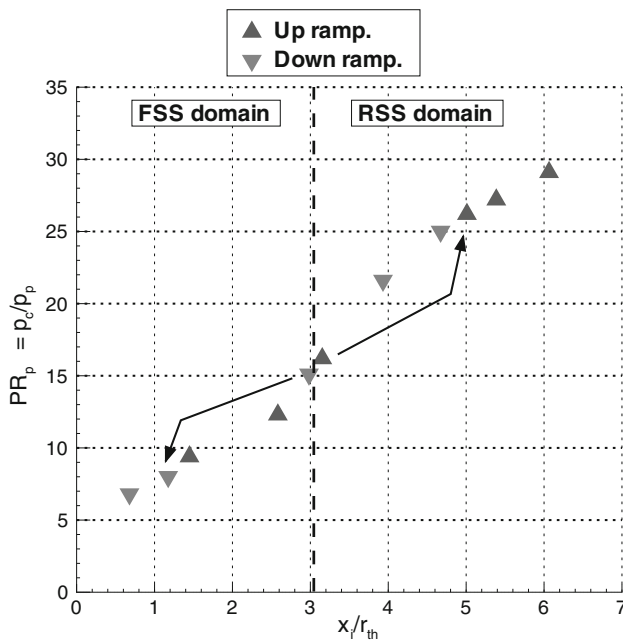
Fig. 14 Non-dimensional separation point abscissa x_i/r_{th} versus the plateau pressure ratio $PR_p = p_c/p_p$

Therefore, the plateau pressure ratio can be used as a parameter to individuate a single point for the transition and re-transition between the separation patterns.

4 Conclusion

The numerical analysis of the two different shock separation patterns that take place in a sub-scale parabolic nozzle has shown that the transition from FSS to RSS, during the startup phase, occurs when the internal shock intersects the separation shock below the triple point, that is when it impinges on the Mach disk. The re-transition happens in a similar way, when the intersection point between the separation shock and the reflected shock reaches the internal shock the RSS pattern changes into FSS pattern. The numerical simulations were also able to reproduce an hysteresis phenomenon in the transition between the free and the RSS patterns, at the same chamber to ambient pressure ratio both solutions can be obtained, depending on the initial condition. The hysteresis can be explained by the lower plateau pressure p_p in the closed recirculation bubble with respect to the FSS case. Therefore, the same nominal $PR = p_c/p_a$ can correspond to two different chamber to plateau pressure ratios $PR_p = p_c/p_p$ with two different values of the separation point abscissa: one in the FSS domain and one in the RSS domain. When considering the ratio PR_p, a single linear correlation with x_i and a single transition point can be individuated.

References

1. Frey, M., Hagemann, G.: Status of flow separation prediction in rocket nozzles. AIAA Paper 98-3619 (1998)
2. Nasuti, F., Onofri, M.: Viscous and inviscid vortex generation during startup of rocket nozzles. AIAA J. **36**, 809–815 (1998)
3. Onofri, M., Nasuti, F.: The physical origin of side loads in rocket nozzles. AIAA Paper 99-2587 (1999)
4. Frey, M., Hagemann, G.: Flow separation and side loads in rocket nozzles. AIAA Paper 99-2815 (1999)
5. Reijasse, P., Morzenski, L., Blacodon, D., Birkemeyer, J.: Flow separation experimental analysis in overexpanded subscale rocket-nozzles. AIAA Paper 2001-3556 (2001)
6. Terhardt, M., Hagemann, G., Frey, M.: Flow separation and side-load behavior of truncated ideal rocket nozzles. AIAA Paper 2001-3686 (2001)
7. Wang, T.-S.: Transient three-dimensional analysis of side load in liquid rocket engine nozzles. AIAA Paper 2004-3681 (2004)
8. Mouronval, A.-S., Hadjadj, A., Kudryavtsev, A.N., Vandromme, D.: Numerical investigation of transient nozzle flow. Shock Waves **12**(5), 403–411 (2003)
9. Deck, S., Guillen, P.: Numerical simulation of side loads in an ideal truncated nozzle. J Propuls. Power **18**, 261–269 (2002)
10. Nasuti, F., Onofri, M., Pietropaoli, E.: The influence of nozzle shape on the shock structure in separated flows. In: Proceedings of 5th European Symposium on Aerothermodynamics for Space Vehicles, 8–11 Nov 2004, vol. ESA SP-563, pp. 353–358 (2005)
11. Hadjadj, A., Onofri, M. (eds): Special issue: nozzle flow separation. Shock Waves **19**(3), 163–169 (2009)
12. Nasuti, F., Onofri, M.: Shock structure in separated nozzle flows. Shock Waves **19**(3), 229–237 (2009)
13. Stark, R., Kwan, W., Quessard, F., Hagemann, G., Terhardt, M.: Rocket nozzle cold-gas test campaigns for plume investigations. In: Proceedings of 4th European Symposium on Aerothermodynamics for Space Vehicles, 15–18 Oct 2001, vol. ESA SP-487, pp. 611–618 (2002)
14. Reijasse, P., Poutrel, R.: Flow separation regimes induced by cap-shock in over-expanded optimized propulsive nozzles. In: Proceedings of European Conference for Aerospace Sciences (EUCASS), Moscow, Russia, 4–7 July 2005, ONERA, Châtillon Cedex, France (2005)
15. Nave, L., Coffey, G.: Sea level side loads in high-area-ratio rocket engines. AIAA Paper 73-1284 (1973)
16. Hagemann, G., Frey, M., Koschel, W.: Appearance of restricted shock separation in rocket nozzles. J Propuls. Power **18**, 577–584 (2002)
17. Deck, S., Nguyen, A.T.: Unsteady side loads in a thrust-optimized contour nozzle at hysteresis regime. AIAA J. **42**(9), 1878–1888 (2002)
18. Nasuti, F., Onofri, M.: Analysis of unsteady supersonic viscous flows by a shock fitting technique. AIAA J. **34**, 1428–1434 (1996)
19. Moretti, G.: Efficient calculations of 2D compressible flows. Adv. Comput. Methods PDE **6**, 60–66 (1987)
20. Paciorri, R.: Sviluppo di una metodologia numerica in forma quasi-lineare e analisi di modelli termochimici per lo studio di flussi viscosi ipersonici. Ph.D. Thesis, Università degli studi di Roma *La Sapienza* (1995)
21. Spalart, P.R., Allmaras, S.R.: A one-equation turbulence model for aerodynamic flows. La Recherche Aerospatiale **1**, 5–21 (1994)
22. Stark, R.H., Hagemann, G.: Current status of numerical flow prediction for separated nozzle flows. In: Proceedings of Second European Conference for Aerospace Sciences, July 2007, Brussels, Belgium
23. Mattsson, J., Högman, U., Torngren, L.: A sub scale test programme on investigation of flow separation and side loads in rocket nozzles.

In: Proceedings of Third European Symposium on Aerothermodynamics for Space Vehicles, 24–26 Nov 1998, vol. ESA SP-426, pp. 373–378 (1998)

24. Wang, T.-S.: Transient three-dimensional startup side load analysis of a regeneratively cooled nozzle. Shock Waves **19**(3), 251–264 (2009)

25. Gross, A., Weiland, C.: Numerical simulation of separated cold gas nozzle flows. J Propuls Power **19**(3), 509–519 (2009)

26. Schmucker, R.: Flow processes in overexpanding nozzles of chemical rocket engines report TB-7,-10,-14, Technical University Munich (1973)

27. Nguyen, A.T., Deniau, H., Girard, S., Alziary De Roquefort, T.: Unsteadiness of flow separation and end-effects regime in a thrust-optimized contour rocket nozzle. Flow Turbul. Combust. **71**(1–4), 161–181 (2003)

28. Stark, R.H., Wagner, B.H.: Experimental flow investigation of a truncated ideal contour nozzle. AIAA Paper 2006-5208 (2006)